

6

Visibility and Cloud Lidar

Christian Werner¹, Jürgen Streicher¹, Ines Leike¹, and
Christoph Münkel²

¹Institut für Physik der Atmosphäre, DLR Deutsches Zentrum für Luft- und
Raumfahrt e.V. Oberpfaffenhofen, D-82234 Wessling, Germany
(christian-werner@gmx.de, juergen.streicher@dlr.de, ines.leike@gmx.de)

²Vaisala GmbH, Schnackenburgallee 41d, D-22525 Hamburg, Germany
(christoph.muenkel@vaisala.com)

6.1 Introduction

Visibility, or visual range, is a property of the atmosphere that has direct significance not just for our pleasure and well-being. Visibility is of decisive importance for all kinds of traffic operations. An uncounted number of victims have been injured or killed because of visibility or, rather, the lack of it. In road traffic a cautious driver can go slowly and stop altogether if, in a snowstorm or in heavy rain or fog, visibility gets worse and worse. This possibility is restricted in boat operations and absent in air traffic.

Unlike *in situ* devices which determine visibility in one point, or fixed installations for the determination of optical transmission between two locations on the ground, lidar allows one to make observations of atmospheric conditions over an extended optical path from one location, fixed or mobile, in any, not just in horizontal direction.

Lidar allows quantitative determination of visual range as a function of distance and is thus ideally suited to measure visibility at airports both over the different parts of runways and in the air space above where aircraft safety depends particularly critically on the pilots' unimpeded view and orientation.

6.2 The Notion of Visual Range

Visual range is in this context defined as a local variable of the atmosphere that is directly related to its turbidity: the higher turbidity, the shorter the visual range.

Visibility is physically limited by two effects: the inability of light from a distant object to reach the eye of the observer due to atmospheric absorption, and the increase of background light from atmospheric scattering between the object and the observer [1]. In other words: an object can no longer be seen by the observer if its apparent brightness gets close to the brightness of the background—exactly how close is a matter of definition as will be shown below.

The magnitude of the former effect is described by the atmospheric absorption coefficient $\alpha(x, \lambda)$ which may depend on range x and which varies with wavelength λ . The magnitude of the latter is determined by the atmospheric backscatter coefficient $\beta(x, \lambda)$. Visibility also depends on the position of the sun, on the color of the object, and on other parameters. α and β are related to each other. For molecular scattering they are strictly proportional, the proportionality factor being $\alpha/\beta = (8\pi/3)$ sr. For particle (cloud and aerosol) scattering they are still proportional, but the factor varies by an order of magnitude with aerosol material, particle size distribution, moisture, and other aerosol properties.

According to Koschmieder's theory [2], visual range V is determined only by the contrast threshold K an observer needs to distinguish an object from its background, and by the extinction coefficient α .

Variations in the relation between α and β and all other effects mentioned are neglected in the simple definition

$$V(x) = \frac{1}{\alpha(x)} \ln \frac{1}{K}. \quad (6.1)$$

The *average* visual range between two points at distance x_1 and x_2 is then given by the obvious relation

$$\bar{V} = \frac{x_2 - x_1}{\int_{x_1}^{x_2} \alpha(\xi) d\xi} \ln \frac{1}{K}. \quad (6.2)$$

Clearly, Eq. (6.1) defines a local and Eq. (6.2) an averaged atmospheric property.

6.2.1 Normal Visual Range

The convention is that α is taken at $\lambda = 550$ nm. At this wavelength visual sensitivity is best. Koschmieder [2] sets $K = 0.02$, the contrast threshold for a normal-sighted, experienced observer. From Eq. (6.1) we thus obtain the normal visual range, or normal optical range

$$\text{NOR} = \frac{1}{\alpha} \ln \frac{1}{0.02} = \frac{3.912}{\alpha}. \quad (6.3)$$

6.2.2 Meteorological Optical Range

For practical purposes a more conservative contrast threshold $K = 0.05$ is assumed, taking into consideration psychological and stress effects to which an observer such as an aircraft pilot may be exposed, leading to the shorter so-called meteorological visual range (or meteorological optical range)

$$\text{MOR} = \frac{1}{\alpha} \ln \frac{1}{0.05} = \frac{3}{\alpha}. \quad (6.4)$$

The definition of *average* NOR and average MOR between two points is fully analogous to the definition of Eq. (6.2).

6.2.3 Vertical Optical Range

Horizontal stratification, or a marked variation of the extinction coefficient with height, is a frequent phenomenon. An observer looking up from the ground can see an object up to a height VOR defined, in analogy to the previous definitions, by the relation

$$\int_0^{\text{VOR}} \alpha(z) dz = 3. \quad (6.5)$$

Vertical optical range VOR is, in other words, the height above ground up to which the extinction coefficient α must be integrated to yield the value 3; from this height one-twentieth of the light reaches an observer on the ground. Or, more important, 1/20 of the light generated at the ground reaches an observer at height VOR (which could be a balloon or aircraft pilot).

6.2.4 Slant Optical Range

Suppose an observer is at a height h above some horizontal plane, which can be a runway or, more generally, the ground. Slant optical range (SOR) is the maximum *horizontal* distance from the point exactly below him on the ground to another point on the ground he can see from his position at height h . With Pythagoras' theorem, we have

$$\text{SOR} = h \left[\left(\frac{3}{\int_0^h \alpha(z) dz} \right)^2 - 1 \right]^{1/2}. \quad (6.6)$$

Slant optical range is thus the projection of a slant line of vision onto the horizontal plane. Clearly, SOR depends on height h . In most cases SOR decreases as h increases. When h reaches and exceeds VOR, the radicand in Eq. (6.6) gets negative, and SOR vanishes.

6.2.5 Runway Visual Range, Slant Visual Range

For the sake of completeness two more quantities are mentioned here, runway visual range (RVR) and slant visual range (SVR) (as opposed to SOR). These quantities are defined by the International Civil Aviation Organization ICAO [3, 4]. RVR is the maximum distance out to which a pilot, from a position 5 m above the runway, can recognize either the runway center line or the lights along the runway, defined again by the projection of the actual optical paths as in Eq. (6.6) onto the runway center line. In daylight, unless the runway lights are very bright, RVR=MOR.

In a similar way a quantity called slant visual range is defined for positions $h \gg 5$ m. Again, if there are no bright landing fires, then SVR=SOR in daylight conditions.

6.3 Visibility Measurements with Lidar

Because of its great importance in air traffic, visibility was one of the first atmospheric quantities to which the lidar technique was applied [5]. As any lidar, visibility lidar also suffered from the problem that two atmospheric quantities, the absorption coefficient α and the backscatter coefficient β , were to be determined from one measured quantity, the lidar signal.

Attempts to work at different measurement angles [6], use several wavelengths [7], and utilize reflections from hard targets [8] did not prove applicable. More sophisticated apparatus such as Raman and high spectral resolution lidar (HSRL) systems were not used because of their complexity in design and operation. The problem was finally solved by using essentially the same procedure as that described in Chapter 4, with the simplification that no separate knowledge of the aerosol and molecule contributions to α and β is necessary, only the total values of the respective quantities, or even of total α alone.

The method starts from the familiar lidar equation

$$P(x, \lambda) = \frac{c \Delta t}{2} P_0 \frac{A \eta O(x)}{x^2} \beta(x, \lambda) \tau^2(x, \lambda) \quad (6.7)$$

with $P(x, \lambda)$ representing the signal power from distance x at wavelength λ , P_0 the average laser power transmitted during the pulse duration Δt , A and η the receiver area and efficiency, O the laser-beam receiver-field-of-view overlap integral, β the backscatter coefficient, and

$$\tau(x, \lambda) = \exp \left[- \int_0^x \alpha(\xi, \lambda) d\xi \right] \quad (6.8)$$

the one-way extinction between the lidar and the distance of interest, x . As simple visibility lidars work at one frequency only, we drop λ in the respective quantities and rewrite Eq. (6.7) to yield

$$P(x) = k \frac{O(x)}{x^2} \beta(x) \tau^2(x). \quad (6.9)$$

We define the quantity

$$S(x) \equiv \frac{P(x)x^2}{kO(x)} = \beta(x)\tau^2(x) \quad (6.10)$$

and solve the differential equation

$$\frac{\partial \ln(S(x))}{\partial x} = \frac{1}{\beta(x)} \frac{\partial \beta(x)}{\partial x} - 2\alpha(x) \quad (6.11)$$

to obtain, with the well-known approximations, the solution

$$\alpha(x) = \frac{S(x)}{\frac{S(x_m)}{\alpha(x_m)} + 2 \int_x^{x_m} S(\xi) d\xi} \quad (6.12)$$

in a procedure fully analogous to the one described in Chapter 4. It must be noted that in the present application the assumptions and approximations made in the solution of Eq. (6.11) hold sufficiently well. Equation (6.12) is thus a stable solution of the profile of the extinction coefficient $\alpha(x)$. To use it, however, the boundary values of S and α at the remote end of the lidar range, $S(x_m)$ and $\alpha(x_m)$, must be known. A data evaluation algorithm stable enough to also work in an automated regime is the following [9, 10]:

- (i) From the signal $P(x)$ of the first measurement of a run, values are determined for the minimum and maximum range for which data evaluation appears meaningful.
- (ii) An initial value of $\alpha(x_m)$ is chosen that is sufficiently large to lead to reasonably stable integration, but must be within the range of extinction coefficients that can be determined with the system. The lower limit of extinction coefficients is given by the signal-to-noise ratio, i.e., by the laser power and the sensitivity of the detector, the upper limit is determined by total extinction and thus, at fixed distance-bin width, by the number of bins.
- (iii) The integration is then carried out within the limits determined according to (i).
- (iv) Values of local visibilities are averaged, rejecting values beyond the limit predetermined in (ii).
- (v) The average is compared with the starting value. If the agreement is within 10%, it is considered the final value. If not, the average is taken for the next starting value, and steps (iii) to (v) are repeated. If this was not successful after 10 iterations, the procedure is stopped with an error message.
- (vi) If the iteration was successful, the resulting value is taken as a starting value for the next run, step (ii).

6.4 Aerosol Distributions

Impaired visibility is always caused by particles in the atmosphere. Particle distributions that frequently affect visibility are conveniently grouped in categories according to their origin, size, and effects. Particle size distributions span a wide range of radii r and are generally described by a modified gamma distribution

$$n(r) = ar^\varepsilon \exp(-br^\gamma) \quad (6.13)$$

or by sums of such distributions each of which is then called a “mode” [11]. $n(r)dr$ is the number volume density of particles with radii between r and $r + dr$. The constants a , b , ε , and γ are all real and positive. ε and γ which describe the steepness of the rise and fall of the distribution are taken as integer and half-integer, respectively. The larger ε and γ , the steeper and narrower the mode. The radius of particles that are most abundant, or mode radius, is given by

$$r_c = \left(\frac{\varepsilon}{b\gamma} \right)^{\frac{1}{\gamma}}. \quad (6.14)$$

The total number density is obtained by integration over all particle radii:

$$N = a \int_0^{\infty} r^{\varepsilon} \exp(-br^{\gamma}) dr. \quad (6.15)$$

When carried out, the integration yields

$$N = a\gamma^{-1} b^{-(a+1)/\gamma} \Gamma((a+1)/\gamma). \quad (6.16)$$

The Γ function is related to the Π function which interpolates the factorials by the relation $\Gamma(k) = \Pi(k-1)$, with $\Pi(0) = \Pi(1) = 1$, $\Pi(2) = 2$, $\Pi(3) = 6$, etc.

In Table 6.1 nine common types of cloud, fog, and haze have been listed along with the parameters that describe particle size distributions if

Table 6.1. Parameters for the particle size distribution for several standard atmospheric conditions

Atmospheric condition	a	ε	b	γ	r_c (μm)	N (m^{-3})
Advection fog heavy	0.027	3	0.3	1.0	10.0	$20 \cdot 10^6$
Advection fog moderate	0.066	3	0.375	1.0	8.0	$20 \cdot 10^6$
Cumulus cloud C1/ Radfog heavy	2.373	6	1.5	1.0	4.0	$100 \cdot 10^6$
Corona cloud C2	$1.085 \cdot 10^{-2}$	8	1/24	3.0	4.0	$100 \cdot 10^6$
Haze H	$4.0 \cdot 10^5$	2	20.0	1.0	0.1	$100 \cdot 10^6$
Haze L	$4.976 \cdot 10^6$	2	15.119	0.5	0.07	$100 \cdot 10^6$
Haze M	$16/3 \cdot 10^5$	1	8.943	0.5	0.05	$100 \cdot 10^6$
Cloud C3	5.556	8	1/3	3.0	2.0	$100 \cdot 10^6$
Radfog moderate	607.5	6	3	1.0	2.0	$200 \cdot 10^6$

this distribution is assumed to be monomode. Four of these parameters, e.g., a , b , ε , and γ , can be taken, independently from one another, from fits to measured distributions. The remaining two are then obtained from relations (6.14) and (6.16). In the table, ε , γ , r_c , and N were taken as primary parameters and a and b were calculated.

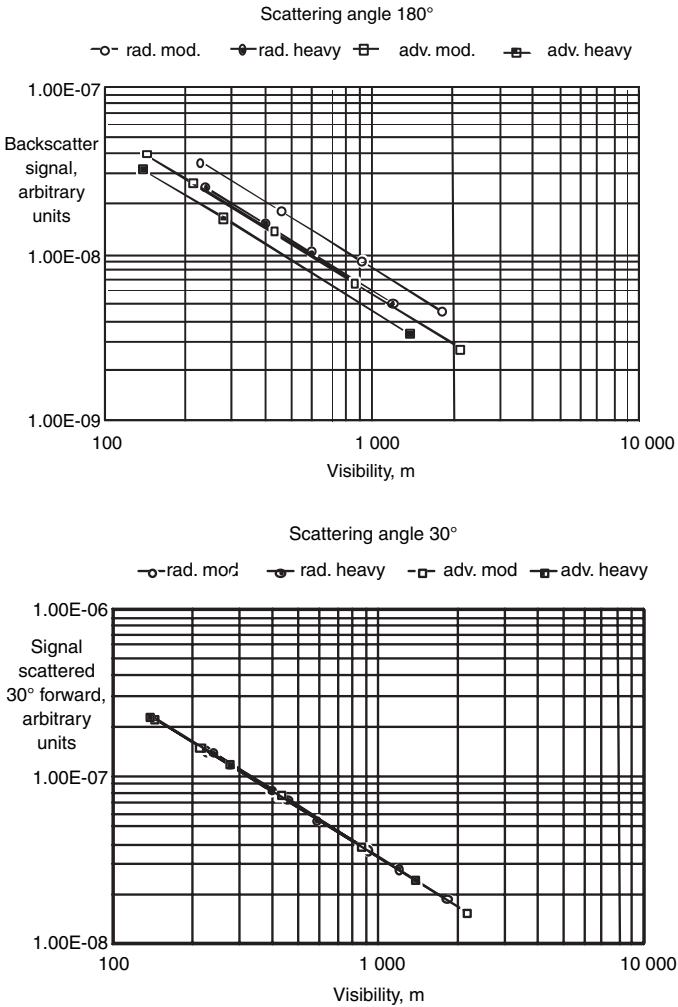


Fig. 6.1. Relative magnitude of scattered signal for four types of fog: radiative moderate, radiative heavy, advected moderate, and advected heavy. Whereas backscatter intensities (top) vary by a factor > 1.5 , 30°-forward scattering is almost identical (bottom).

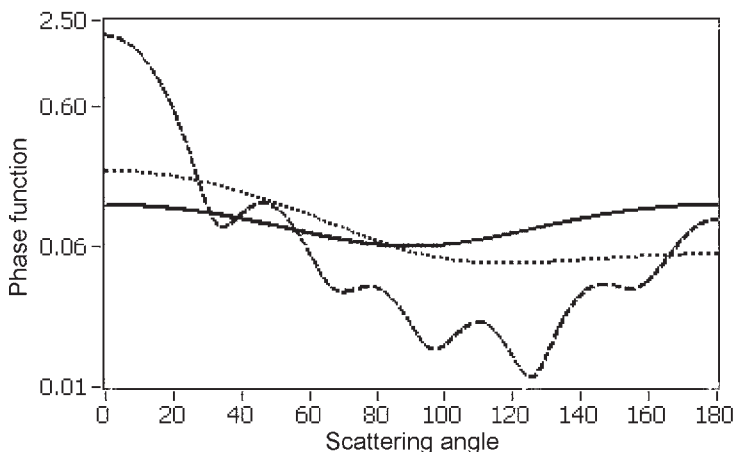


Fig. 6.2. Phase functions of spherical particles of different size. Solid line: 1 nm radius (Rayleigh scattering), dotted line: 100 nm, dashed line: 500 nm (Mie scattering). Scattering wavelength is 550 nm, index of refraction 1.55.

Much like the size distributions, the scattering phase functions—or scattering amplitudes—as a function of angle are also different for different weather conditions. For lidar, the scattering angle of relevance is 180° . Indeed, backscatter intensities vary by more than a factor of 1.5 for different fog conditions (Fig. 6.1, top). It is interesting to note that at a forward scattering angle of 30° these differences nearly vanish (Fig. 6.1, bottom). This is also seen in Fig. 6.2, which gives the scattering phase functions I for spherical particles of three different sizes. These functions are normalized such that the integral is unity:

$$\int_{\varphi=0}^{2\pi} \int_{\cos \vartheta=0}^1 I(\varphi, \vartheta) \, d \cos \vartheta \, d\varphi = 1. \quad (6.17)$$

6.5 Visibility and Multiple Scattering

In dense media, especially in clouds, the backscattered lidar signal may have undergone more scattering processes than just the near- 180° backscatter process. Multiple scattering (Chapter 3) may strongly affect visibility measurements. The extent to which multiple scattering contributes to the lidar signal depends on the properties of the particles (size and volume number density, optical depth) and on the geometry of the lidar: the larger the volume from which light is detected, the

larger the multiple-scattering contribution. The fraction of multiply scattered light therefore increases with laser beam divergence, receiver field of view, and increasing distance between the lidar and the scattering volume.

Lidars are usually characterized by low beam divergence and a narrow receiver field of view. As large particles scatter light predominantly in the forward direction (cf. Fig. 6.2), the first scattering process occurs more often than for smaller particles in such a way that the scattered light is still within the lidar FOV so that it can directly be backscattered towards the receiver. Therefore large particles have the greatest share in multiple scattering.

Multiple scattering thus results in a reduction of the apparent extinction coefficient and a seemingly longer visual range. The effect is taken into account by appropriate correction terms for dense media.

The contribution of multiple scattering from dense media to the lidar return signal can be quite large. For illustration, Fig. 6.3 shows a simulated lidar return from a C1 cloud, 300 m thick, at a distance of 2000 m, and the relative contributions from single, double, and triple scattering events.

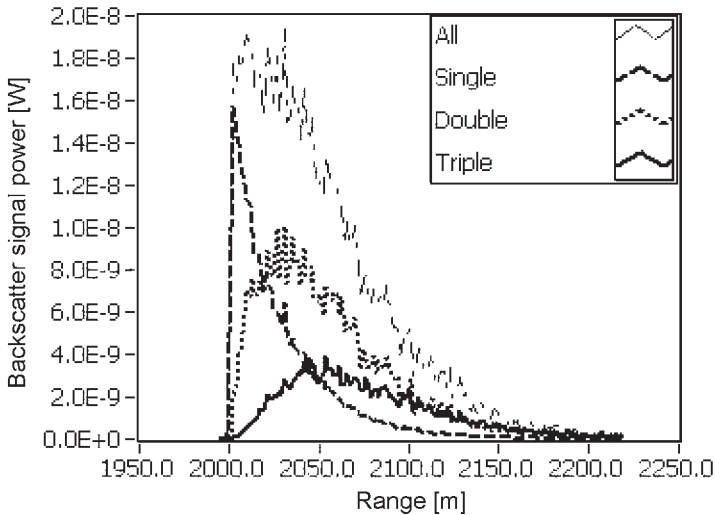


Fig. 6.3. Simulated lidar return signal from a C1 cloud of 300 m geometric depth at a distance of 2000 m. Dashed: single-scattering, dotted: double-scattering, solid: triple-scattering contribution to the total signal (light vertical bars).

6.6 Instruments

Visibility lidars are essentially backscatter lidars. Their sophistication is more in light weight, small volume, reliability, ruggedness, and ease of operation than in the ultimate in power, bandwidth, etc. Visibility lidar systems are commercially available from several manufacturers. Because they can also be used for other purposes such as cloud height detection and aerosol measurements, they often come under different names.

A family of systems particularly well suited for visibility measurements are the different types of Ceilometers provided by the Vaisala Company. Figure 6.4 shows such a system in operation at Oberpfaffenhofen, Germany.

The instrument transmits, at a wavelength around 900 nm, pulses of 30 W average power with a pulse repetition frequency of 6 kHz. The laser beam, expanded to 100 mm diameter, meets class-1M eye-safety criteria. One vertical aerosol profile (and thus one visibility profile) is produced

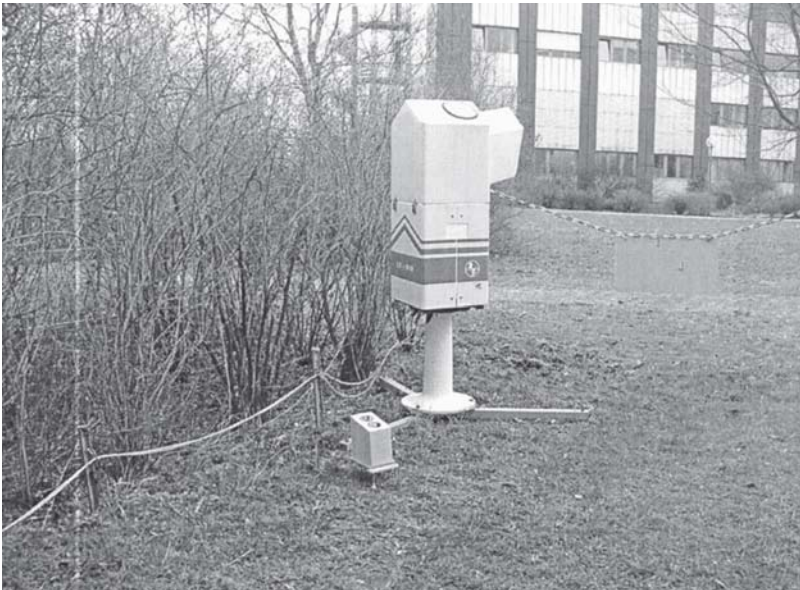


Fig. 6.4. Modified Impulsphysik (Vaisala) Ceilometer at Oberpfaffenhofen airstrip (see <http://www.op.dlr.de/ipa/lidar-online>). Photograph also shows (left and in front of Ceilometer) the smaller WHM1k model (cf. Subsection 6.8.2).

every 30 s, although only 10,000 shots per profile are needed. The system is fully automated and can produce horizontal and slant profiles as well, 24 hours a day.

6.7 Applications

Range-resolved recording of the backscattered signal allows the depth-resolved measurement of turbidity and, thus, of the local visibility as defined in Eq. (6.1), for distances between several meters and a few kilometers, depending on weather. From that all secondary quantities, whether integrated or not, can be determined. A number of examples is presented below for illustration.

6.7.1 Meteorological Optical Range (MOR) at Hamburg Airport

During a campaign at the airport of Hamburg, Germany, in 1991 a visibility lidar was installed near the touchdown point. Figure 6.5 shows 1.5 hours of lidar data along with the results from a standard transmissometer. Although the MOR data varied by more than a factor of 2.5 during the measurement time, the two sets of data are practically identical with, on average, a slight tendency of the lidar to be lower than the transmissometer data (by $\leq 15\%$) and thus on the safe side.

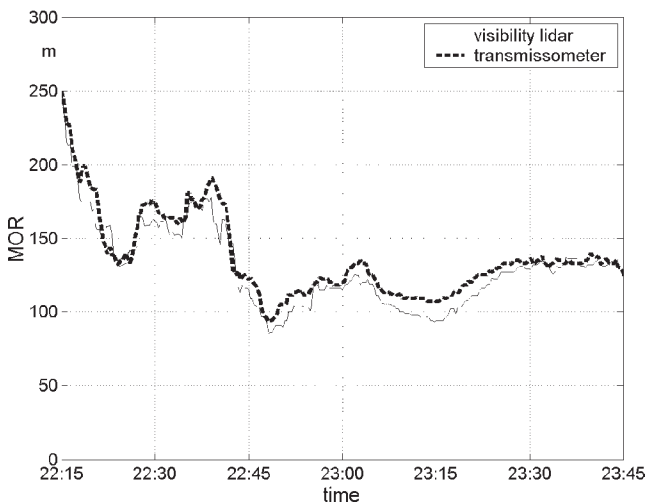


Fig. 6.5. Visibility MOR versus time for two sensors, a standard transmissometer and a visibility lidar (airport Hamburg, Germany, 12 January 1992).

6.7.2 Slant Visibility (SOR) at Quickborn

Slant visibility SOR (Eq. 6.6) is particularly important for aircraft landing approaches in situations of ground fog and lifted fog layers. A campaign to compare MOR and SOR was staged in Quickborn, Germany, from 1988 to 1990. Two transmissometers, one slant and one horizontally oriented, were used between two masts. A visibility lidar measured from the same position into several elevation angles. The arrangement of the instruments is sketched in Fig. 6.6. Figure 6.7 shows results obtained in three different fog situations. In the event of Fig. 6.7(a) we have relatively homogeneous fog which starts to evaporate around 07:05. Slant visibility SOR increases from about 80 m to more than 1000 m thirty minutes later and is almost identical to the meteorological optical range MOR. In Fig. 6.7(b) a thin layer of fog on the ground affects the horizontal transmissometer, but not the slant instruments which yield much higher visual range values. This is the typical situation in which pilots can see the runway or landing lights but are not allowed to land because the ground transmissometer indicates too dense fog on the ground [3]. Figure 6.7(c) shows the opposite situation in which the fog has lifted from the ground, resulting in good visibility on the ground but poor slant-path visual range [12].

6.7.3 Detection of Clouds

Visibility lidars are very well suited for the detection of clouds down to an optical thickness that is hard to perceive with the naked eye from below.

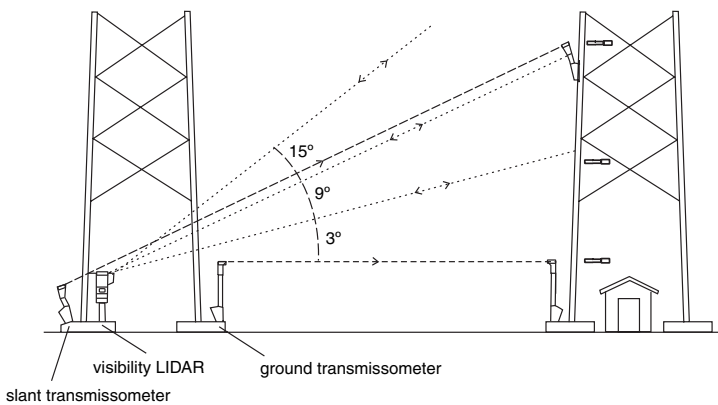


Fig. 6.6. Measurement scenario for comparison of horizontal (MOR) and slant visibility (SOR).

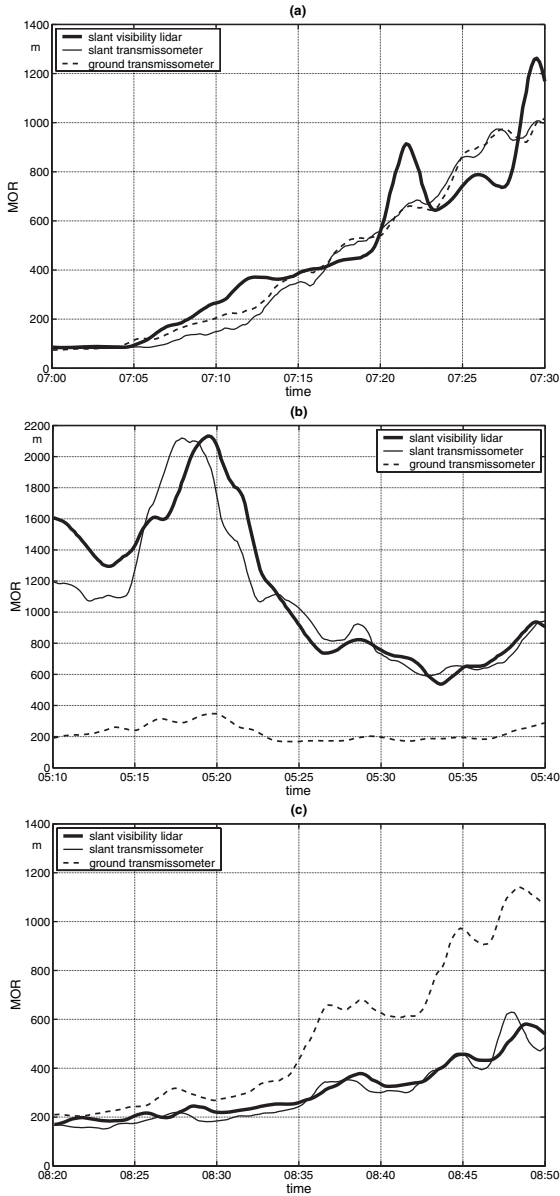


Fig. 6.7. Comparison of horizontal (MOR) and slant visibility (SOR). The optical path of the ground transmissometer was at a height of 2 m. The slant transmissometer measured at an elevation angle of 9° . The distance between the transmitter and receiver of the transmissometers was roughly 50 m. The lidar elevation angle was alternated between 3, 9, and 15° . For the comparison the lidar data set was calculated at an elevation of 9° .

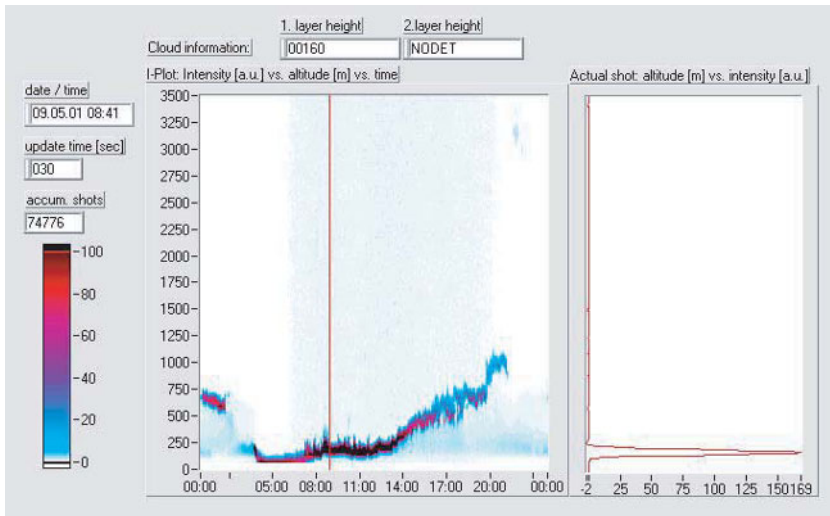


Fig. 6.8. Screenshot of vertical fog profile measurements from 8 May 2001, 08:42, to 9 May 2001, 08:41. The plot at right is the actual lidar signal.

Figure 6.8 shows a color-coded intensity plot of the optical density as a function of altitude and time, in a sequence of one profile every 30 s. The red vertical bar is the actual time (08:41 in this case), the data to the right of the red line are the results of the previous day. The seamless transition to the profiles 24 hours before is purely accidental. The actual height profile of the lidar signal is shown on the right. We note the presence of fog and of clouds most of the time, at an altitude that varies between less than 100 m in the early morning and about 1200 m around 20:00 hours. Although the measurement range of the system is 3500 m, the signal gets extinct after 250 m because of the dense fog layer which starts at 160 m altitude.

6.7.4 Cloud Ceiling

Figure 6.9 gives an example of two cloud layers appearing in the profile from a standard commercial ceilometer, illustrating the ability to detect high cirrus clouds.

The standard reporting frequency of ceilometers in use at airports is one set of data every 15 s. An automatic cloud algorithm investigates the shape of the backscatter profile, discards maxima originating from signal noise or falling precipitation, and generates a data message with cloud

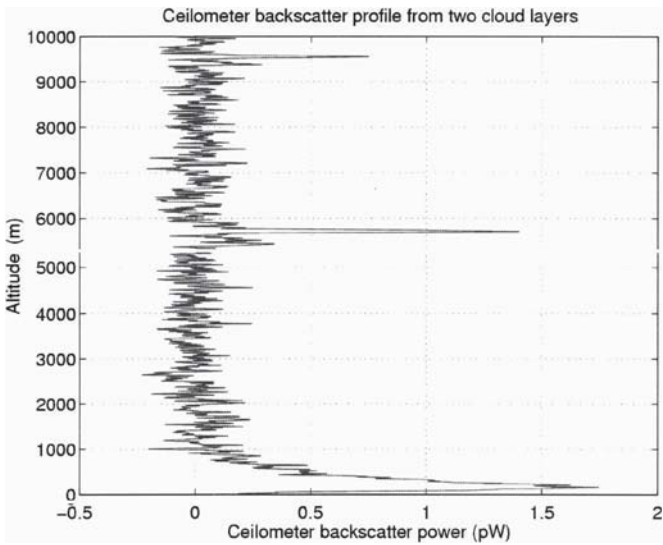


Fig. 6.9. Ceilometer backscatter signal from boundary layer aerosol and two cloud layers with base heights of 5700 m and 9600 m. Profile taken with a Vaisala LD-40 Ceilometer on 13 May 2001, 22:15:16 – 22:16:46, averaged over 382,752 pulses.

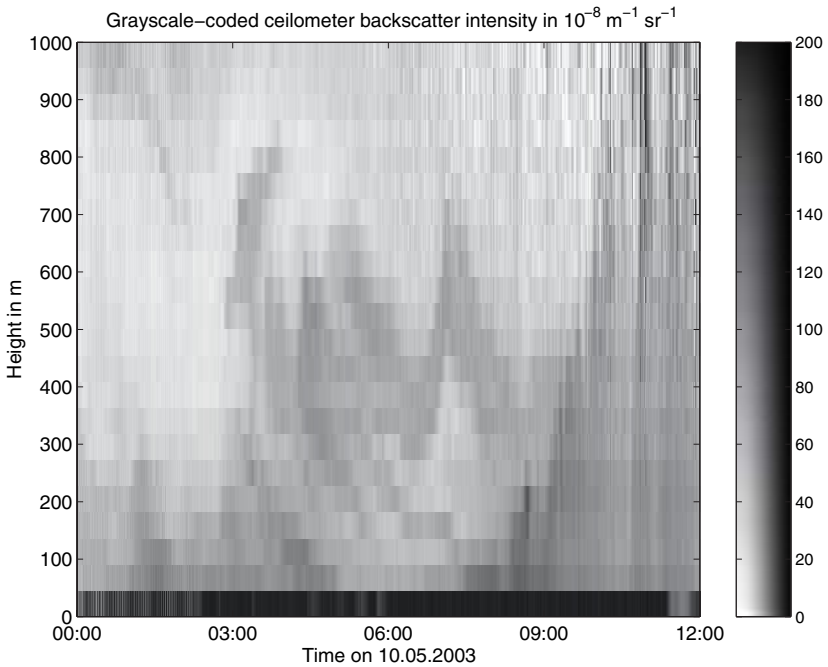


Fig. 6.10. Grayscale-coded intensity plot of range-corrected ceilometer backscatter profiles (Hamburg, Germany, 10 May 2003).

base heights and instrument status information. Additional parameters reported include vertical visibility and the amount of precipitation.

Even in clear-atmosphere situations like the one prevailing in Fig. 6.9 there is enough backscatter signal detected from altitudes up to 1000 m to estimate the aerosol concentration in the planetary boundary layer.

6.7.5 Mass Concentration Measurements

When the visual range exceeds 2000 m, a standard ceilometer designed to detect cloud bases still receives a considerable amount of backscatter signal from boundary-layer aerosol. The grayscale-coded intensity plot in Fig. 6.10 gives an example.

Comparisons with *in situ* sensors measuring dust concentration values (PM10 and PM2.5) show a good correlation between ceilometer signal and dust concentration measured in the corresponding altitude [13]. Figure 6.11 shows this relationship using an empirically derived

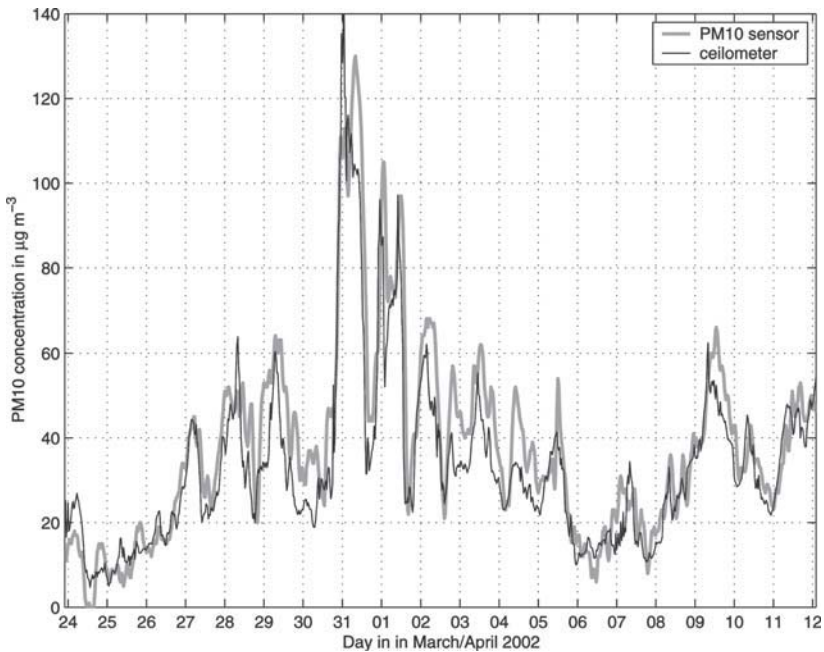


Fig. 6.11. Dust concentration derived from ceilometer backscatter between 0 and 30 m altitude and PM10 concentration between 0 and 20 m height (Hannover, Germany, 24 March to 12 April 2002).

linear dependency between ceilometer backscatter and PM10 mass concentration.

6.8 Recent Developments

6.8.1 Intelligent Taillight: Adaptation of Brightness Using the Lidar Technique

Although in many regions road traffic density has increased dramatically, the rate of accidents has generally decreased. A good deal of this trend is due to the development of equipment that increases traffic safety. The continuation of this process thus deserves particular attention [14, 15].

The perceptibility of automotive lighting and light signals under poor visibility conditions is one important field in this context. The problem is not just precipitation and fog. On a wet road spray whirled up by tires also affects visibility quite strongly. Depending on the amount of moisture on the road and on driving speed, this spray is dragged like a flag more than 20 m behind the vehicle. A measuring principle based on spot-like scanning of only a small volume is not suited for the initialization of any countermeasures. Rather, a method is needed that can measure the turbidity in an extended measuring volume. The exact size of that volume may have to be adapted to the vehicle's speed.

To help improve the visibility of vehicle rear lights to the driver of the vehicle behind, a system is under development for installation in automobile taillights that must be able to detect the following parameters:

- visibility reduction by rain, snow, fog or tire spray,
- distance of the following car and
- speed of the following car.

The sensor data are then transferred to a unit called rear light controller (RLC) in which these and other automotive data are linked to a weather model to generate control signals that regulate the brightness of the lamps. The complete lidar system consists of a transmitter (a laser diode and an optical lens), a receiver (an optical lens and an avalanche photodiode) and a data acquisition system (a digitizer and microcomputer). The whole system including the electronic lamp brightness regulator is housed in a box the size of a car radio. The first prototype is shown in Fig. 6.12 built into the rear part of an automobile. The

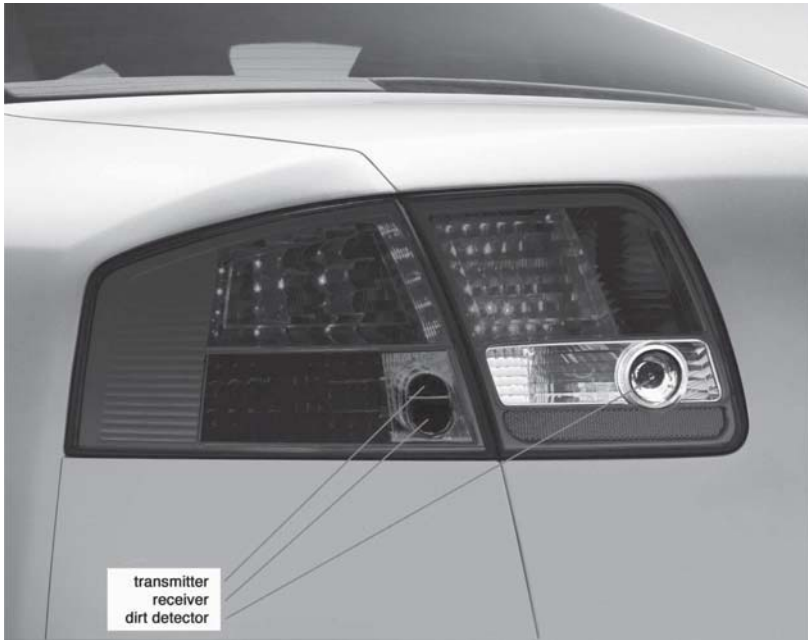


Fig. 6.12. Intelligent taillight for automobiles.

integration of the lidar data into a taillight-control computer program and tests in an artificial smoke chamber have been carried out, with very satisfactory results.

6.8.2 Miniaturized Visual-Range Lidar for Heliports

In addition to airports where there is generally no serious limitation of space, heliports on boats, drilling platforms, hospital buildings, and the like also need information on cloud base height and visibility. For this purpose a miniaturized visual-range lidar was developed by Jenoptik [16]. The system with model designation WHM1k is considerably more compact than current ceilometers. The difference becomes evident from Fig. 6.4 which shows a WHM1k installed adjacent to an Impulsphysik (Vaisala) standard ceilometer at the DLR site Oberpfaffenhofen.

As can be seen in Fig. 6.13, the two instruments yield essentially the same results. Figure 6.13 also shows that the smaller instrument, which has been designed for shorter operating range, performs very well in situations in which helicopters can still land safely, while safe landing

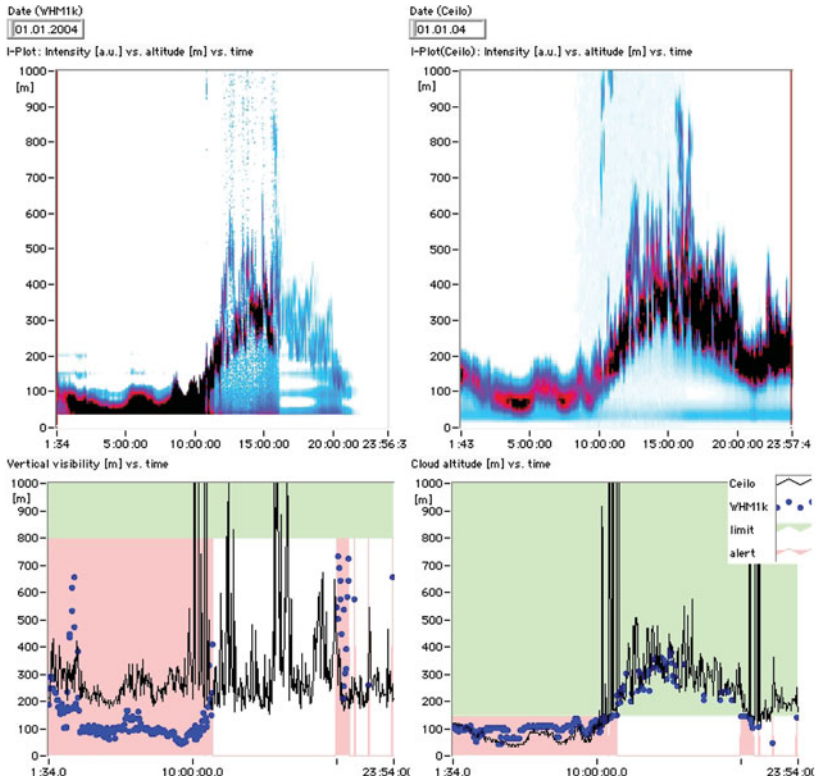


Fig. 6.13. WHM1k optical-density plot from 8 January 2004.

of an airplane would be a considerable challenge. It clearly indicates, however, visibility conditions too poor for a landing approach of the helicopter as well, as is the case between 01:34 and 10:10 in the graph. Figure 6.13 shows the fog recording from 8 January 2004.

Both devices clearly ‘see’ ground fog with patches of varying density from midnight to approximately 11:00. During that time the inversion and cloud detection algorithm registers alarm conditions from the data of both systems: cloud altitude is below 150 m, and vertical visibility is below 800 m. The numerical differences in vertical visibility between the WHM1k (about 100 m) and the ceilometer (about 300 m) are caused by the AC-coupled detection unit of the WHM1k sensor. The smooth signal from the homogeneous fog layer is interpreted as a DC background and cut off by the 1-kHz high-pass filter of the receiver electronics.

From Fig. 6.13 it can also be seen that the fog layer starts to rise at approximately 11:00 hours. The ceilometer still measures some impairment of local visibility, but as this happens at altitudes above 150 m, VFR (i.e., visual flight rule) conditions still prevail. The WHM1k cloud-altitude algorithm follows the rise of the cloud, which seems to become thinner in the WHM1k density plot (top left), but not in the ceilometer plot (top right). This effect occurs only at night. The reason is the fact that the sensitivity control of the APD current is carried out using the background light information. This also needs to be improved. We thus see that downscaling a well-tested, trustworthy, and reliable system still constitutes a technological challenge.

6.9 Summary

In summary it can be stated that visibility lidar is an accepted technology wherever impaired vision must be detected to impose speed limits to road or takeoff and landing restrictions to air traffic. Visibility lidars known as ceilometers have reached a degree of maturity to work 24 hours a day in the required fully-automated, hands-off operation mode. The development of much smaller systems for use under restricted space conditions and of systems small and cheap enough to be used as a truck and car accessory is in progress, with good chances to reach full commercial availability soon.

References

- [1] W.E.K. Middleton: *Vision through the Atmosphere* (University of Toronto Press, Toronto 1952)
- [2] H. Koschmieder: Beiträge zur Physik der freien Atmosphäre **12**, 33 (1924)
- [3] ICAO (International Civil Aviation Organization): *Manual of Runway Visual Range Observing and Reporting Practices* (Doc 9328-AN/908), Toronto, 2000
- [4] World Meteorological Organization: *Guide to Meteorological Instruments and Methods of Observation*. Sixth Edition, p. 1.9.1, Geneva, 1996
- [5] R.T.H. Collis, W. Viezee, E.E. Uthe, et al.: Visibility measurements for aircraft landing operations. AFCRL Report – 70-0598 (1970) – also FAA document DoT-FA70WAI-178
- [6] G.J. Kunz: Appl. Opt. **26**, 794 (1987)
- [7] J.F. Potter: Appl. Opt. **26**, 1250 (1987)
- [8] R.B. Smith, A.I. Carswell: Appl. Opt. **25**, 398 (1986)
- [9] German Patent DE 196 42 967 C1 (1998)
- [10] VDI Guideline **VDI 3786** Part 15: Visual-range lidar (Beuth Verlag, Berlin 2004)

- [11] D. Deirmendjian: *Electromagnetic Scattering on Spherical Polydispersions* (Elsevier, New York 1969)
- [12] J. Streicher, C. Munkel, H. Borchardt: *J. Atmos. Oceanic Tech.* **10**, 718 (1993)
- [13] C. Munkel, S. Emeis, W.J. Müller, et al.: *Proc. SPIE* **5235**, 486 (2004)
- [14] J. Streicher, C. Werner, J. Apitz, et al.: *Europto Proceedings* **4167**, 252 (2001)
- [15] R. Grüner, J. Schubert: *Proc. SPIE* **5240**, 42 (2004)
- [16] J. Streicher, C. Werner, W. Dittel: *Proc. SPIE* **5240**, 31 (2004)